RSC Advances

PAPER

View Article Online
View Journal | View Issue

Cite this: *RSC Adv.*, 2023, **13**, 23590

Polarizability characteristics of twisted bilayer graphene quantum dots in the absence of periodic moiré potential

Xiangyue Liu,[a] Xian Wang,[b] Shengping Yu,[c] Guangzhao Wang,[d] Bing Li,[a] Tiantian Cui,[a] Zhaoyang Lou*[a] and Hong Ge*[a]

Recent studies have documented a rich phenomenology in twisted bilayer graphene (TBG), which is significantly relevant to interlayer electronic coupling, in particular to the cases under an applied electric field. While polarizability measures the response of electrons against applied fields, this work adopts a unique strategy of decomposing global polarizability into distributional contributions to access the interlayer polarization in TBG, as a function of varying twisting angles (θ). Through the construction of a model of twisted graphene quantum dots, we assess distributional polarizability at the first-principles level. Our findings demonstrate that the polarizability perpendicular to the graphene plates can be decomposed into intralayer dipoles and interlayer charge-transfer (CT) components, the latter of which provides an explicit measurement of the interlayer coupling strength and charge transfer potential. Our analysis further reveals that interlayer polarizability dominates the polarizability variation during twisting. Intriguingly, the largest interlayer polarizability and CT driven by an external field occur in the misaligned structures with a size-dependent small angle corresponding to the first appearance of AB stacking, rather than the well-recognized Bernal structures. A derived equation is then employed to address the size dependence on the angle corresponding to the largest values in interlayer polarizability and CT. Our investigation not only characterizes the CT features in the interlayer polarizability of TBG quantum dots, but also sheds light on the existence of the strongest interlayer coupling and charge transfer at small twist angles in the presence of an external electric field, thereby providing a comprehensive understanding of the novel properties of graphene-based nanomaterials.

Received 23rd May 2023
Accepted 1st August 2023

DOI: 10.1039/d3ra03444e

rsc.li/rsc-advances

1. Introduction

Graphene-based geometries, including monolayers, bilayers, and multilayers, have great potential for use in photo-electromagnetic devices due to their attractive properties.[1–3] Intriguingly, the properties of bilayer graphene (BG) change profoundly at a relative twist angle between two component layers, so-called twisted bilayer graphene (TBG), resulting in a variety of interesting phenomena of superconductivity,[4–6] correlated insulators,[7,8] moiré bands and Hofstadter's butterfly spectra,[9] van Hove singularities (VHSs),[10] *etc.* These unique properties are highly relevant to the strong interlayer coupling, which has been expounded in depth through numerous theoretical investigations.[11–13] Interlayer rotation, leading to various stacking patterns to form periodic moiré potential, significantly affects the interlayer coupling and thus determines the physical properties of TBG. However, many applications of bulk graphene are thwarted by possessing a zero bandgap.[14–16] Actually, when 2D graphene sheets are converted into 0D quantum dots (QDs), to a certain extent, it extends varieties of characteristic properties and new phenomena owing to the remarkable size- and shape-dependent energy levels in electronic structure and optical absorption or emission spectra induced by the quantum confinement and edge effects.[17–19]

Recent advances in the exploration of graphene quantum dots (GQDs) have indicated their extensive potential as distinctive physicochemical and biological entities, serving as a novel platform in various fields including nanomedicine, biotechnology, cancer therapy and quantum information processing,[20–23] *etc.* Specifically, GQDs, owing to their excellent biocompatibility, are ideal imaging probes in diverse modalities of bioimaging, such as fluorescence, *in vivo* optical and nuclear magnetism imaging.[24,25] In addition, compounded with rapid response of photoluminescence-based GQDs and photostability, GQDs have emerged as promising biosensors for ion

[a]*The Affiliated Cancer Hospital of Zhengzhou University, Henan Cancer Hospital, Zhengzhou 450008, China. E-mail: louslove@163.com; zlyygehong0199@zzu.edu.cn*

[b]*Institute of Atomic and Molecular Physics, Key Laboratory of High Energy Density Physics of Ministry of Education, Sichuan University, Chengdu 610065, China*

[c]*School of Chemistry and Environment, Southwest Minzu University, Chengdu 610041, China*

[d]*School of Electronic Information Engineering, Key Laboratory of Extraordinary Bond Engineering and Advanced Materials Technology of Chongqing, Yangtze Normal University, Chongqing 408100, China*

and small molecule detection, and as diagnostic platforms platform.[26,27] Furthermore, GQDs exhibit high photothermal conversion ability in addition to intrinsic photoluminescence properties, enables their application in tumor imaging and tracking in cancer therapy.[28] The small size of GQDs facilitates their rapid clearance from the body, thereby demonstrating excellent biosafety.[29] Varieties of functional groups on the edge of GQDs can be integrated with therapeutics and targeting ligands. Moreover, the sp^2-hybridized carbon in the lattice allows therapeutic molecules to be restricted to the planes of the GQDs, which promotes the drug loading capacity and enhances the efficiency of drug release. It can be thus applied to biosensing, including photodynamic therapy, drug delivery and gene delivery.[28,30,31] In particular, considerable attention has been focused on the development of efficient radiosensitizers with low toxicity in radiation therapy (RT). Radiosensitizer can release the hypoxia in the tumor area through augment the reactive oxygen species (ROS) formation and DNA damages that significantly enhance the radiation treatment. Nevertheless, the clinical application of many conventional metal radiosensitizers with a high atomic number such as gold and gadolinium nanomaterials still faces many obstacles, particularly the high preparation cost, complicated purification technology and systemic toxicity.[32] Recently, the non-metal GQDs with highly augmented photoluminescence properties and biocompatibility has received remarkable scientific attentions as a promising radiosensitizer in the field of RT. Abundant surface oxygen-containing groups facilitate the overproduction of ROS and mitochondrial damage, thereby promoting the radiation response.[33,34] Consequently, constructing, functionalizing, and doping GQDs are essential for their impact on biological, electronic, magnetic, and optical properties.

Numerous investigations have been conducted on GQDs-based systems with a focus on their diverse properties of monolayer and bilayer graphene quantum dots (BG QDs).[2,3,19,24,35–37] The manipulation of the particular properties of these materials can be achieved through various means, such as altering and controlling the relative twist between two stacked GQD flakes, which results in the emergence of exotic physicochemical properties, quasi-crystalline order, and emergent correlated effects. For instance, Berashevich *et al.*[38] applied two stacked graphene flakes by an interlayer twist to investigate the interlayer coupling of TBG flakes, finding that repulsion, decoupling and enhanced coupling appear at different exact twist angle. Mirzakhani *et al.*[39] investigated the effect of twisting angle on the energy levels of TBG QDs at the absence of magnetic field, demonstrating that the dependence between the electronic structures and stacking patterns. In addition to interlayer twist, the introduction of an external electric field perpendicular to the BG QDs layers is also an effective tool to manipulate the interaction coupling effect and the charge rearrangement between the constituent layers. Many desirable properties of bilayer graphene and its QDs are induced at an external electric field,[7,8,40–43] which can be detected, controlled and measured by experiments. In recent years, significant progresses in preparation and characterization on TBG QDs have become available. Many experiments have synthesized BG by physicochemical methods,[44,45] to gain their QDs by cutting techniques,[46,47] and to precisely control their interlayer twist angle.[48]

Polarizability serves as a valuable tool to explore the electron response to an external field, thereby enabling the study of response behavior of bilayer graphene quantum dots with a relative interlayer twist to an external electric field. In order to evaluating the competitive relationship between the intra- and inter-layer contributions upon the external applied field, a polarizability partitioning scheme is adopted based on density functional theory calculations, decomposing the total polarizability into atomic contributions – namely, intra- and inter-layer counterparts of polarizability.[49] The TBG QDs twist angle dependences of, energy, band gap, charge flow behavior and polarization, including total, intra- and inter-layer parts, and atomic charge variation induced by an external field, are analyzed systematically in this work. Our investigation on the size- and interlayer twist-mediated polarizability characteristics in TBG QDs demonstrates that controlling the stacking pattern of layered-materials is a serviceable pathway to realize fascinating physicochemical and biological properties and provide a deep insight on design of novel graphene-based devices to further extend their applications.

2. Methodology

In this study, we utilize four coronene-based monolayer GQDs composed of 13, 37, 73, and 121 carbon atoms, each with 9, 15, 21, and 27 terminal hydrogen atoms, to construct twisted bilayer GQDs, as illustrated in Fig. 1. Each monolayer contains a single valence electron and is situated parallel to the *xy* plane. The influence of interlayer distances on the strength of interlayer coupling has been discussed in previous work.[49,50] It is worth noting that an optimized interlayer distance of approximately 3.34 Å (ref. 51 and 52) is adopted to the fixed GQDs samples in experiments. Consequently, we treat the GQDs with an equilibrium interlayer distance of 3.34 Å in the following calculations. Compared to the stationary bottom layer, the top layer of the quantum dot (QD) is rotated by an angle θ around one of the carbon (C) atoms located in the central six-membered ring, as depicted in Fig. 1(a). The constructed interlayer twist configurations are created by fixing the bottom layer and twisting the opposite layer about the carbon atoms of the innermost cycle from 0° to 60° at an interval of 1°, which are respectively denoted as TBG_{44}, TBG_{104}, TBG_{188} and TBG_{296} depending on their total number of atoms. The stacking patterns vary with twisting, which are categorized as AA, SP and AB stackings. One corresponds to AA stacking, where the C atoms in the top layer is right above the atoms in bottom layer. In the AB stacking, atoms in top layer position above the center of six-rings in the bottom layer. Meanwhile, the SP stacking pattern is considered as the intermediate between AA and AB stackings. Fig. 1(b) depicts the optimized geometrical TBG systems with different sizes at $\theta = 0°$ (AA stacking) and 60° (full-AB stacking). Similar models were built in ref. 49 and 50 in which the monomers are extended phenalenyls, and the

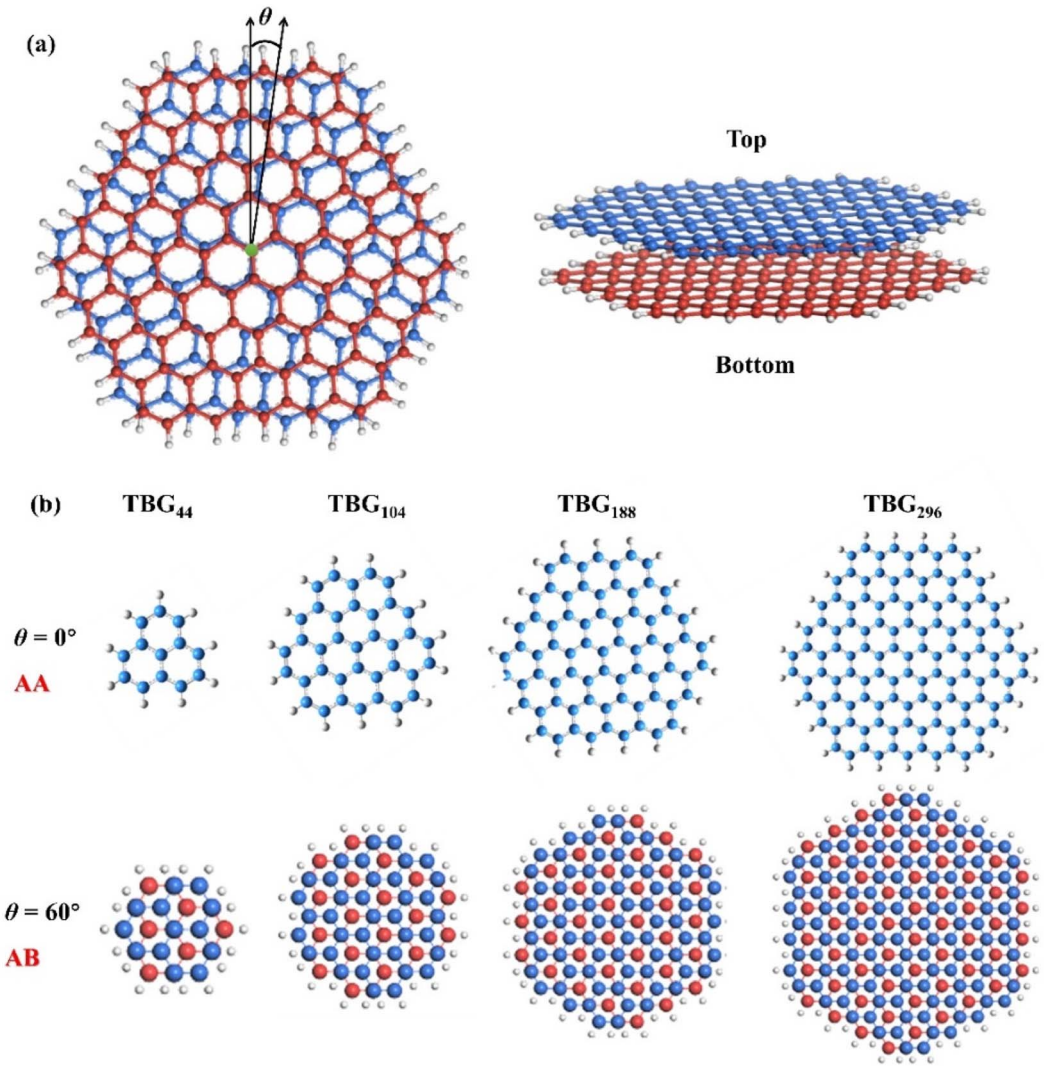

Fig. 1 (a) Top and side view of a twisted bilayer graphene quantum dot (TBG QD) characterized by a specific twisting angle denoted as θ. (b) The top-view diagram of the four constructed TBG_N configurations with a twist angle of $\theta = 0°$ and 60°, named AA and AB stacking patterns respectively. Blue and red balls represent carbon atoms of different component layers respectively.

rotation axis passes through the center of the innermost six-membered ring.

All the first-principles calculation results presented in this paper are evaluated within the spin-polarized density functional theory (DFT) framework, as implemented in Gaussian 16 package,[53] including the geometric optimization, energetic and electronic properties under the effect of the external electrical field. The influence and reliability of dispersion correction for functional and the diffuse functions for basis set on the polarizability of GQDs have been explored in ref. 49 and 54. "To accurately describe the long-range and van der Waals interlayer coupling in the twisted bilayer structures of different sizes, the functional CAM-B3LYP[55] including long-range correction and Grimme's D3 correction[56] and the standard Gaussian-type basis set 6-31G(d,p)[57] are employed to study the TBG QDs with different sizes.

Electron delocalization in a layered configuration has two origins, intra and inter contributions respectively. The intra-layer part derives from electron redistribution on two sides of the layer. The inter-layer part involves the overlap of electron cloud of the two layers, or electron flow between them. To differentiate the intra- and inter-layer contribution counterparts, a polarizability partitioning scheme has been developed to decompose the total polarizability into distributional contributions. The TBG QD is decomposed into two parts, the top and the bottom contributions, along their symmetric *xy* plane. One has

$$\alpha_{zz} = \alpha^{P}_{zz,T} + \alpha^{P}_{zz,B} + \alpha^{Q}_{zz} \quad (1)$$

where α^{P} denotes the intra-layer polarizability and α^{Q} the inter-layer polarizability. B and T denote the bottom and top layers, respectively. Both the intra- and inter-layer polarizability are evaluated with a finite field approach. The field strength is adopted 0.001 a.u., which produces adequate accuracy in numerical differentiation.

$$\alpha_{zz,\mathrm{B(T)}}^{\mathrm{P(Q)}} = \left.\frac{\mathrm{d}\left(\sum_{i\in \mathrm{B(T)}} \mu_{i,z}^{\mathrm{P(Q)}}\right)}{\mathrm{d}F_z}\right|_{F_z\to 0} \quad (2)$$

where

$$\mu_{i,z}^{\mathrm{P}} = \int (r_z - r_{i,z}^0) w_i(\mathbf{r}) \rho(\mathbf{r}) \mathrm{d}\mathbf{r} \quad (3)$$

$$w_i(\mathbf{r}) = \frac{\rho_i^0(\mathbf{r})}{\sum_i \rho_i^0(\mathbf{r})} \quad (4)$$

and

$$\mu_{i,z}^{\mathrm{Q}} = r_{i,z}^0 q_i = r_{i,z}^0 \int w_i(\mathbf{r}) \rho(\mathbf{r}) \mathrm{d}\mathbf{r} \quad (5)$$

where $\rho(\mathbf{r})$ is the electron density at $\boldsymbol{r}$, r_i^0 is the position of atom i, and q_i is the atomic net charge. Additionally, $\rho_i^0(\mathbf{r})$ is the pre-molecular density. Based on Hirshfeld approach,[58] the electron density can be divided into atomic contribution, in which the density is partitioned according to a weight factor (w_i) calculated from $\rho_i^0(\mathbf{r})$ of the individual atoms.

3. Results and discussion

3.1 Configuration stability and intrinsic electronic property

Before elucidating the polarizability characteristics, it is essential to delve into relative structural stability of TBG QDs with diverse size. The relative energy of TBG_N systems is significantly dependent on the interlayer twisting. Taking the structure of $\theta = 0°$ as a reference, Fig. 2(a) displays the dependence of the twist angle on the average relative energy (ΔE_{ave}) of TBG QDs between untwisted and twisted structures. For each size, it is found that the highest energy of ΔE_{ave} is located at the untwisting point ($\theta = 0°$), corresponding to the full-AA stacking pattern, and the energy decreases rapidly as the angle twists away from $\theta = 0°$. It is found that ΔE_{ave} of TBG_{44}, TBG_{104}, TBG_{188} and TBG_{296} decreases to the first local minimum (θ_{E}) around 41°, 22°, 15° and 11°, respectively. θ_{E} decreases with increasing of the TBG QD size. After θ_{E}, ΔE_{ave} remains conspicuous oscillations until $\theta = 60°$, at which the full-AB stacking (Bernal structure) with the lowest energy is achieved. During interlayer twisting, the number of local minima of ΔE_{ave} varies with QD size. Specifically, there is 1, 2, 3 and 4 local minima points of the average relative energy for the TBG_{44}, TBG_{104}, TBG_{188} and TBG_{296} systems, respectively. For instance, the TBG_{188} structure has a relative local minimum ΔE_{ave} value that exists simultaneously at $\theta = 15°$, 35° and 60°. Meanwhile, the differences between those local energy minima and maxima values are approximately the same for all the given sizes. Moreover, the QD model with the smallest size has the most stable structure at θ_{E} rather than $\theta = 60°$ due to the strong effect of the terminal hydrogen atoms. While for TBG_{104}, the ΔE_{ave} values corresponding to $\theta = \theta_{\mathrm{E}}$ and 60° are almost equal. And for the other two configurations with larger sizes, the ΔE_{ave} reaches the greatest negative value at $\theta = 60°$, indicating that the terminal effect deceases with QD size. The results are in good agreement with the previous reports that full-AB stacking is the most stable stacking pattern for bilayer graphene.[38,59,60] The ΔE_{ave} variation is similar to those found in the phenalenyl-based models.[50] Using high-level *ab initio* calculations, Cui *et al.*[61] computed the interaction energy of TBG_{44} in both the singlet and triplet states, finding that the energy landscape depends closely on the electron configuration and interlayer distance. While the minima occur at 0° and 60° in the singlet state, the energy peaks at 0° in the triplet state and decreases with the twist angle. The potential of energy surface becomes flat at $\theta = 30$, 45 and 60°. Our findings suggest that in addition to the well-known Bernal structures, there are many analogous local energy minima for TBG QDs with different sizes in the process of interlayer twisting. That is, the stabilities of TBG QDs at some immediate angles can be compared to that of the most stable Bernal structures.

Furthermore, the implementation of an interlayer twist in the BG QD structures has been established as a convenient method to manipulate their intrinsic electronic characteristics. Fig. 2(b) illustrates the evolutions in the energy gap ($\Delta\varepsilon$) between the highest occupied spin-orbitals (HOSO) and the lowest unoccupied spin-orbital (LUSO) of the TBG_N systems with increasing rotation angle, ranging from 0° to 60°. Our

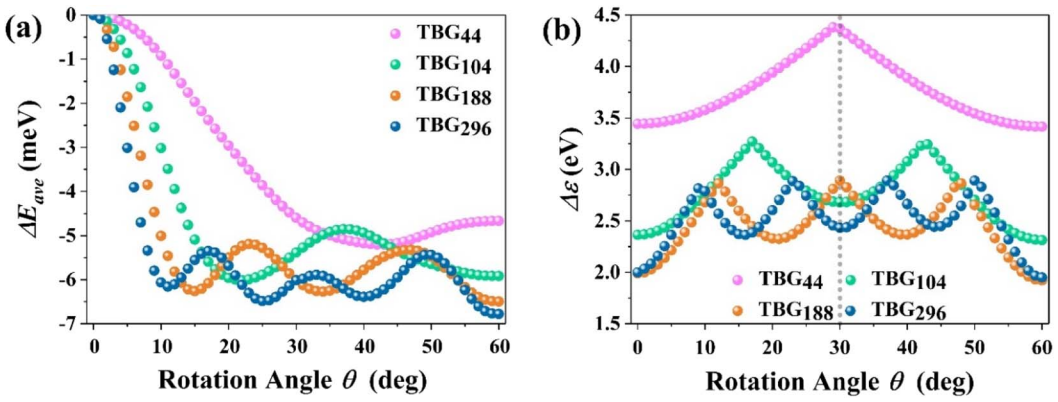

Fig. 2 (a) The variation diagram of the average relative energy (ΔE_{ave}) of TBG_N ($N = 44$, 104, 188 and 296) as a function of the rotation angle θ from 0° to 60°. (b) Variation of the HOSO–LOSO gap ($\Delta\varepsilon$) of TBG QDs *versus* twist angle.

results clearly demonstrate that the band gaps of the all four studied sizes have an obvious twisting dependence, in which the variation trends have a six-fold rotating symmetry with a mirror symmetry of $\theta = 30°$. Therefore, we can clearly obtain the twist and size dependence of band gap when an interlayer rotation in the range from 0° to 30° is exerted, which plays a significant role in practical engineering of the unique functionality of TBG QDs-based optoelectronic devices. The $\Delta\varepsilon$ of TBG_N increases rapidly upon twist, and then reaches their varieties of local minima and maxima, among which the number of local maxima is 1, 2, 3 and 4 for TBG_{44}, TBG_{104}, TBG_{188} and TBG_{296}, respectively. At this point, $\Delta\varepsilon$ reaches the first local maximum (θ_g) at approximately 30°, 17°, 12° and 9° for the four models, with the respective value of 4.37, 3.27, 2.86 and 2.81 eV. The size-dependent band gap can be attributed to the weak quantum confinement effect in the QD systems with larger size, leading to a reduction in $\Delta\varepsilon$ with increasing QD size. Furthermore, $\Delta\varepsilon$ of TBG_{44} maintains a continuously rising trend with the increasing twisting angle when θ deviates from 0°, and displays a downward trend once θ is exceeds 30°, that the values of $\Delta\varepsilon$ are larger than those of other larger sizes at varying rotation angles. For the other three sizes, the local minima values are almost identical for corresponding size except for $\theta =$ 0° and 60°, and the similar trend is observed for the local maxima, while the difference of $\Delta\varepsilon$ among TBG_{104}, TBG_{188} and TBG_{296} decreases with QD size. The above results reveal that the intrinsic electronic properties of TBG QDs depends strongly on the rotational symmetry as well as twist angle, which regularly alter the relative positions of carbon atoms between the two constituent graphene layers.

3.2 Axial polarizability in the direction perpendicular to the QD plates

The twist angle (θ) dependence of the axial polarizability (α_{zz}) for TBG QDs is further investigated to explore the electron response behavior to an external field applied in the direction perpendicular to the QDs plane. Fig. 3(a–d) displays the calculated α_{zz} variations of TBG_N *vs.* twist angle. α_{zz} increases instantly when θ leaves 0°, arrives at the first maximum (θ_P), then reduces rapidly to a local minimum, and then remains a strong fluctuation with twisting until $\theta = 60°$. Obviously, α_{zz} strongly depends on twist angle and QD size. Upon twist, α_{zz} reaches the first peak with maximum value of 107, 268, 492 and 778 a.u. for TBG_{44}, TBG_{104}, TBG_{188} and TBG_{296}, respectively, suggesting that the constructed TBG QDs are the mesoscopic systems with marked quantum size effect that the corresponding α_{zz} is much stronger with the QDs size increasing. What's more, θ_P of those four sizes locates at about 32°, 18°, 12° and 9°, respectively, decreasing with the increase of QD size. Besides the effect on the magnitude of α_{zz}, QD size also has a strong effect on polarizability fluctuations during twist. The number of α_{zz} local minima/maxima varies regularly with the change of the QD size, which corresponds to 1, 2, 3 and 4 for TBG_{44}, TBG_{104}, TBG_{188} and TBG_{296}, respectively. For TBG_{188} and TBG_{296} bilayers, the

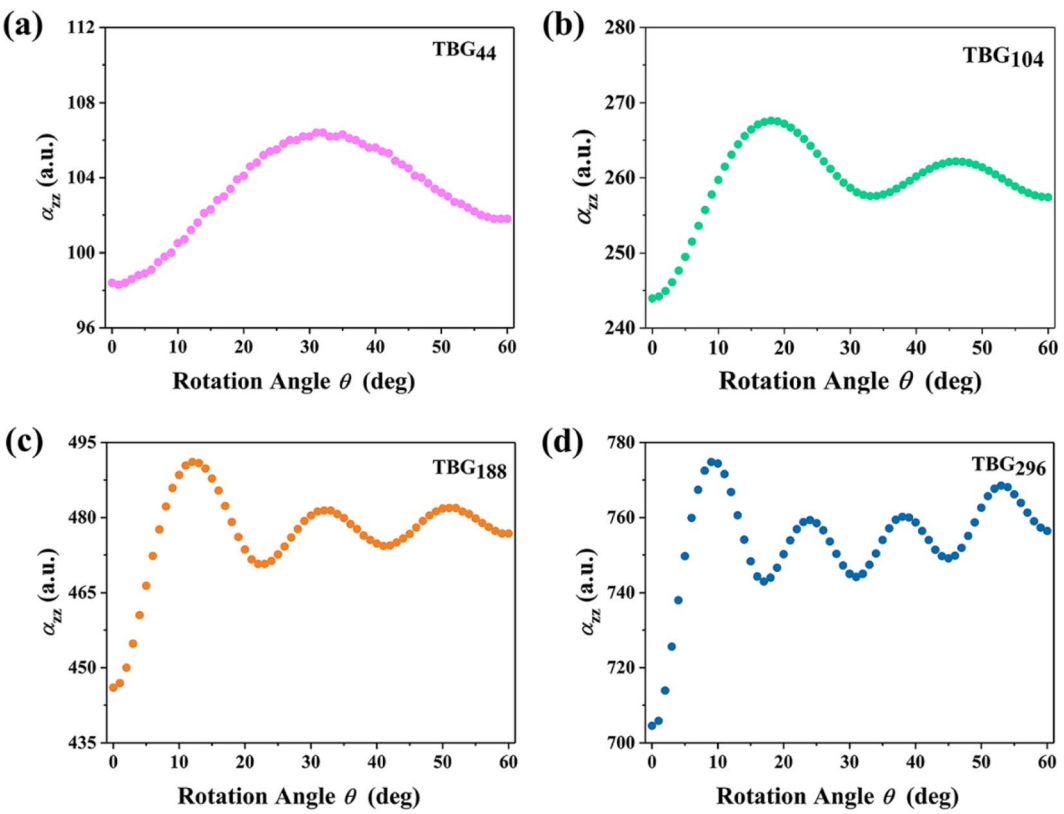

Fig. 3 (a–d) The axial polarizability (α_{zz}) of the constructed TBG QDs varies as a function of twist angle (θ).

amplitude of following fluctuations gradually increases with the increasing rotation angles after reaching the largest polarizability at θ_P.

In general, the transition of HOSO and LUSO states from $\theta = 0°$ to $\theta = \theta_P$ implies the electron density rearrangement between electron donor to electron acceptor states. The relative displacement of carbon atoms between the two constituent layers induced by the interlayer rotation allows for the diverse interlayer stacking patterns in TBG QDs, in which $\theta = \theta_P$ corresponds to the immediate stacking order between the full-AA and full-AB structures. The dependence of HOSO and LUSO displacements on the electric field direction implies that the orbital distribution between the two layers of twisted graphene quantum dots is non-uniform. Fig. 4(a) illustrates the distribution of HOSO and LUSO orbitals (Kohn–Sham orbitals) of TBG_{104} at 0° and θ_P rotation angles under the presence of an external electric field, which can be attributed to the interlayer coupling effect in TBG configurations. The HOSO and LUSO of both twisted and untwisted structures are mainly contributed by the C-p_z orbitals on the conjugated carbon rings. In the case of AA stacking ($\theta = 0°$), the p_z orbitals of one layer interact with those of the other layer. Interlayer coupling is weaker due to the forbidden overlap of the HOSO in stacked TBG materials with opposite phases. Conversely, interlayer coupling is stronger due to the allowed overlap of the LUSO in stacked TBG with identical phases. When the twist angle is θ_p, the p_z orbitals of the upper layer moves towards the six-membered ring of the lower layer, forming a favorable p–π interaction that enhances interlayer coupling. In the twisted structure, significant interlayer orbital overlap is observed for both the HOSO and LOSO states distributions. In the twisted structure, the interlayer coupling resulting from p–π interactions reduces the HOSO and enhances the LUSO, leading to further separation between the HOSO–LUSO. As a result, the twisted structure has a larger $\Delta\varepsilon$ value compared to the non-twisted structure, confirmed by Fig. 2(b). Overall, an interlayer rotation is mainly responsible for the energy gap transition through changing the charge density overlapping, originating from a decrease of the energy level of HOSO and an increase of the energy level of LOSO states. Fig. 4(b) also clearly shows the configurations of the given four TBG QDs with a twist angle of θ_P.

Furthermore, Fig. 5 shows the average axial polarizability $\left(\overline{\alpha_{zz}}, \frac{\alpha_{zz}}{N}\right)$ of TBG_N. The $\overline{\alpha_{zz}}$ value of TBG_{44} is much smaller than that of those three larger structures. The enhanced $\overline{\alpha_{zz}}$ can be observed in the other three larger TBG_N, which implies that those three sizes in the z-direction possess promoted ability of electron rearrangement under an external electric field. $\overline{\alpha_{zz}}$ at θ_P increases with increases of QD size, while the difference decreases with size. In addition to the first peak, the rest of local maxima/minima of $\overline{\alpha_{zz}}$ for TBG_{104}, TBG_{188} and TBG_{296} coincide in some twist angles varying with size, showing small difference among them. The phenalenyl-based models[49] exhibit similar

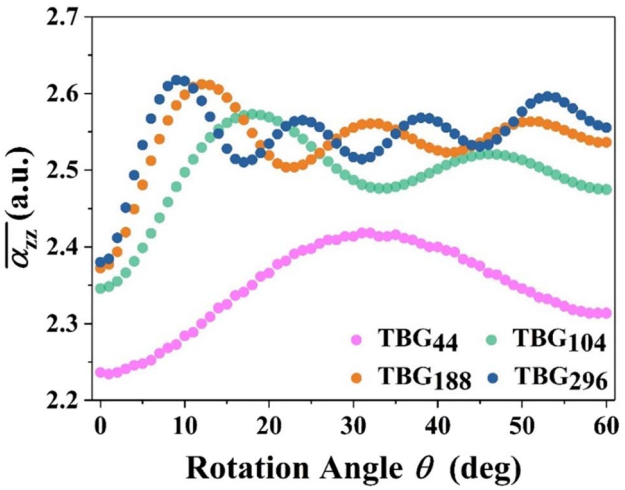

Fig. 5 The average axial polarizability ($\overline{\alpha_{zz}}$) of TBG QDs as functional of twist angle (θ).

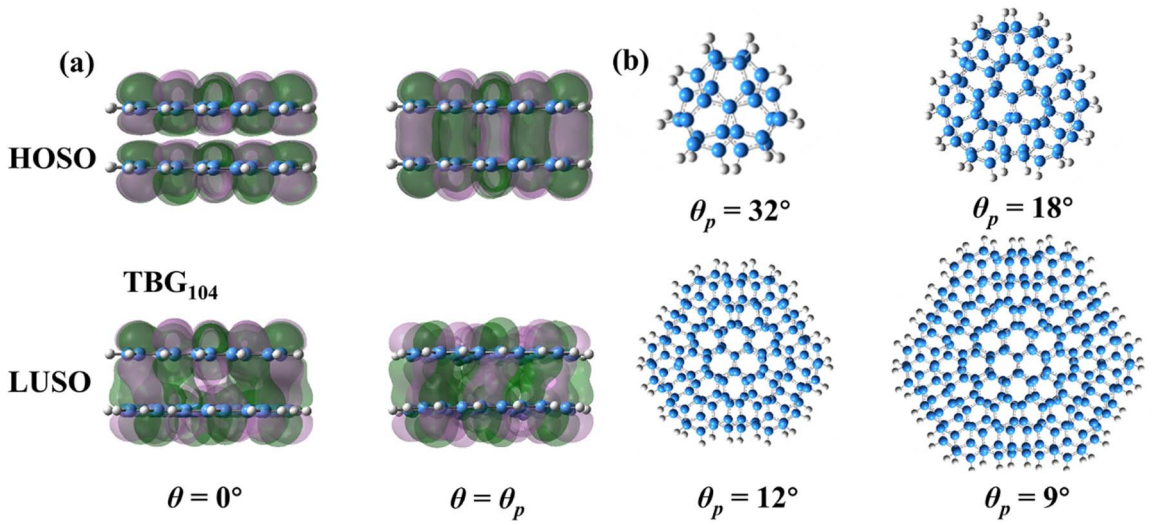

Fig. 4 (a) The distribution of HOSO and LUSO orbitals for TBG_{104} system at $\theta = 0°$ and θ_P. (b) The equilibrium configurations of TBG QDs at θ_P.

variation in $\overline{\alpha_{zz}}$, although the polarizability components are to some extent different in magnitude. It is understandable that the unpaired electrons exhibit a different delocalization effect from those in a closed shell, which usually leads to different polarization responses.

Interestingly, α_z and its $\overline{\alpha_{zz}}$ reach the largest value at size-dependent θ_p, corresponding to the first occurrence of AB stacking in the outmost cycle. In this case, the GQD's diameter (D) and its corresponding location for the appearance of largest α_{zz} (θ_p) can be used the following geometry relation:[49]

$$D = \frac{d}{\sin(\theta/2)} \quad (6)$$

where d is the carbon bond length. Using eqn (6), the twist angle with largest α_z appears for those three larger GQD models can then be predicted as 16.4°, 11.0° and 8.2°, matching well with the calculated values of 18°, 12° and 9°, as shown in Fig. 3. It is evident that for larger size quantum dots, the given geometric relation can predict more accurately the twist angle corresponding to the appearance of the largest peak of $\overline{\alpha_{zz}}$.

3.3 Decomposed intra- and interlayer polarizability

Interlayer coupling is crucial for many intriguing novel properties of twisted bilayer graphene, especially under an external electric field. Actually, interlayer polarizability is an important knob to explore the interlayer coupling when an external filed is perpendicularly applied to the stacking plane of TBG. Intralayer polarization is derived from the charge redistribution on both sides of each layer, while the interlayer polarization comes from electron redistribution between constituent layers. The decomposed intra- and interlayer components, α_{zz}^{P} and α_{zz}^{Q}, of TBG_N are shown in Fig. 6. α_{zz}^{P} has a large value but slight variations during twisting, reducing by 0.61%, 1.63%, 2.36% and 2.58% for TBG_{44}, TBG_{104}, TBG_{188} and TBG_{296}, respectively, indicting the intralayer part dominates in α_{zz} but keeps almost unchanged during twist. It is surprising that α_{zz}^{Q} increases by 46.52, 58.25, 63.42 and 65.86%, respectively, and remains almost similar trend as well as possesses the same local maxima and minima with those of α_{zz}. Taking the largest size as an example, α_{zz}^{Q} increases rapidly at small θ, comes to its first peak at 9°, drops and reaches the first minimum at about 15°, thereafter, arrives at other local maxima (22°, 37° and 52°) and minima (30°, 45° and 60°). Similar variations also occur for the phenalenyl-based models.[49] It is evident that both of the variation gradients of α_{zz}^{P} and α_{zz}^{Q} relative to untwisted structures increase with size, showing high dependency on QD size. The result manifests that the variation of axial polarizability in the z direction is dominated by interlayer counterpart during rotating. The enhanced interlayer polarization highly depends on the stacking patterns.

Upon twisting, the relative displacements of carbon atoms in the opposite layer result in various stacking patterns with diverse interlayer couplings. For full-AA stacking, carbon atoms sit right above the carbon atoms in the opposite layer, resulting in the strongest interlayer repulsion and the smallest α_{zz}^{Q}. Once θ stays away from 0°, the carbon atoms in the outmost cycle

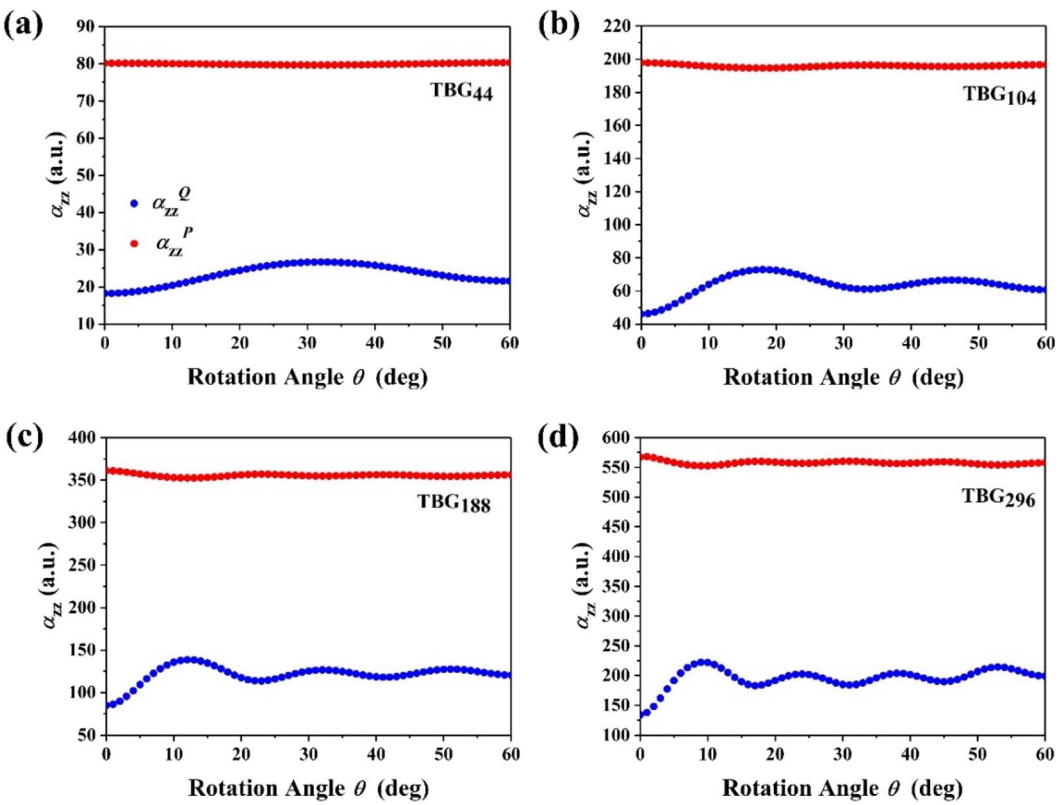

Fig. 6 (a–d) The intralayer polarizability (α_{zz}^{P}, red) and interlayer part (α_{zz}^{Q}, blue) of TBG as functional of twist angle.

gradually move to the center of the six-membered ring, making the weakening of repulsive interaction and increasing of interlayer attraction. α_{zz}^{Q} reaches the largest value at θ_p when AB stacking firstly appears at the outmost cycle to being a mixture of AA, SP and AB stackings. After θ_p, the coupling becomes more complexed because the next outmost and other cycles begin to form AB stacking. Especially, α_{zz}^{Q} at $\theta = 60°$ is a local minimum rather than a maximum, indicating that α_{zz}^{Q} is not just determined by van der Waals interaction, but other electronic coupling. Therefore, the mixing proportion of AA, SP and AB stackings is crucial for the interlayer coupling of TBG QDs owing to the absence of periodic moiré potential.

3.4 Average atomic charge (dq/dF) from inner to outmost cycle

According to eqn (2)–(5), one can decompose the interlayer polarization into atomic contributions. Because $\mu_{i,z}^{P}$ is coordinate-related, it can be defined as follow:

$$\gamma = \delta q^i/\delta F_z \tag{7}$$

$$\gamma_{ave} = \sum_i^N \delta q^i/\delta F_z, \tag{8}$$

where γ represents the variation of the net charge of atom i driven by an external electric field. δq^i and δF_z denote the variation of the net charge of ith atom and the external field, respectively. N is the total number of the atoms in each cycle. γ_{ave} is the average γ in each cycle. Actually, γ is a crucial term in α_{zz}, which is thus applied to evaluate the atomic contribution to α_{zz}^{Q}. Each layer of the four constructed TBG$_N$ models can be decomposed into $2m + 1$ (m = 1, 2, 3, 4) cycles, respectively. Fig. 7 presents the γ_{ave} of each cycle for the structures of θ = 0–60°. For those four sizes, each cycle of γ_{ave} variation increases upon twist, in which innermost and second innermost cycles show a little different trend for corresponding larger three sizes of α_{zz} and α_{zz}^{Q}, while other cycles have the similar trends. At a specific QD size, the outmost cycle possesses the largest γ_{ave} and the next outmost cycle is the second largest, while that of the other cycles present small difference among them during twist. For example, largest γ_{ave} in the innermost cycle is found at θ = 32°, 45°, 48° and 51° for TBG$_{44}$, TBG$_{104}$, TBG$_{188}$ and TBG$_{296}$, with the value of 0.10, 0.13, 0.15, 0.16 a.u., respectively, while largest γ_{ave} in the outermost cycle appears to $\theta = \theta_p$, whose values are 0.25, 0.33, 0.37 and 0.40 a.u., respectively.

In order to deeply investigate the atomic contribution to α_{zz}^{Q}, TBG$_{296}$ is selected to proceed further analyze. Fig. 8 depicts the twist angle dependence on the carbon atomic γ of this system. γ for all the atoms presents the similar trend with α_{zz}^{Q} until around $\theta = \theta_p$. Thereafter, γ for some atoms have much different trends with that of α_{zz}^{Q}. It is noted that the γ variations for most atoms are multifarious at larger twist angle (θ > 35°). For example, at θ = 60°, some atoms in the outmost cycle have smallest γ, while some atoms have largest γ, even higher than that of at $\theta = \theta_p$. The results demonstrate that α_{zz}^{Q} highly relies

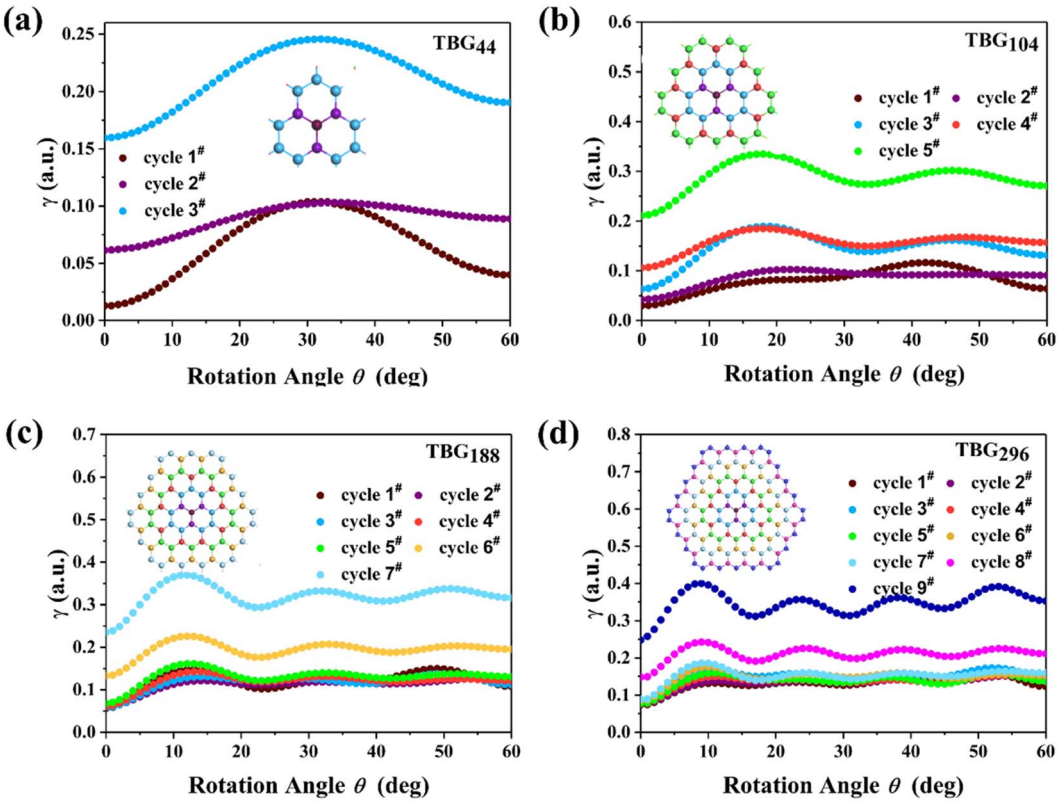

Fig. 7 (a–d) Averaged atomic γ of each cycle of TBG$_N$ as functional of twist angle. The TBG$_{44}$, TBG$_{104}$, TBG$_{188}$ and TBG$_{296}$ configurations are grouped into 3, 5, 7 and 9 cycles respectively, distinguished by color.

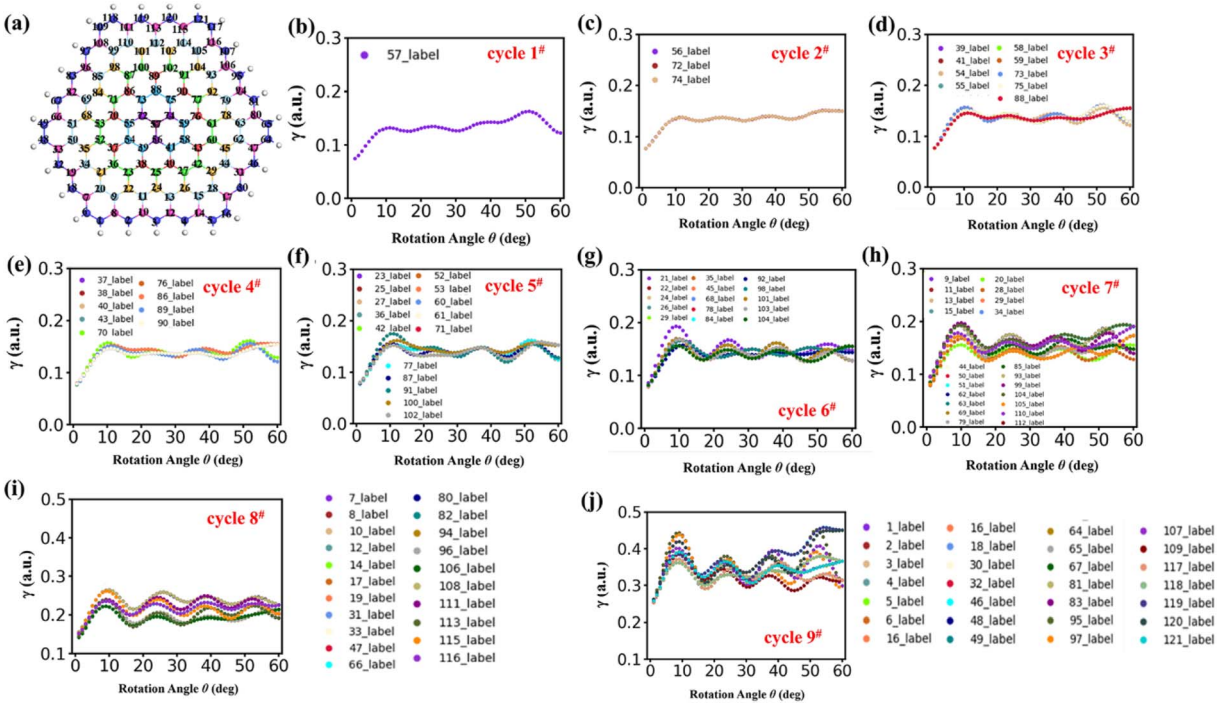

Fig. 8 (a) Presents the top layer of TBG_{296} with the labelled atom number. (b–j) The atomic γ of TBG_{296} in the top layer of cycle $1^{\#}$–cycle $9^{\#}$ with twisting.

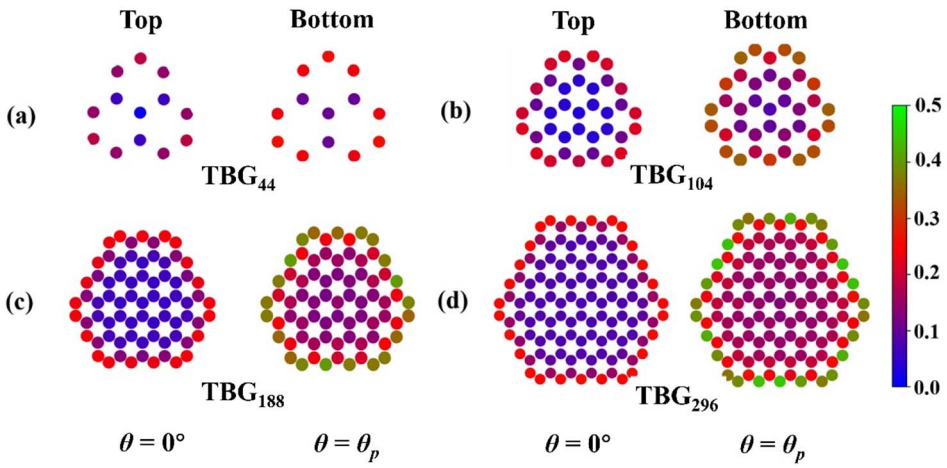

Fig. 9 The atomic γ (in a.u.) of in the top and bottom layer of (a) TBG_{44}, (b) TBG_{104}, (c) TBG_{188} and (d) TBG_{296} at $\theta = 0°$ (left) and θ_p (right).

on the relative atomic position. Furthermore, Fig. 9 displays the γ for carbon atoms of TBG_N at $\theta = 0°$ and θ_p. Atoms in different cycles have different γ, which has similar values in the inner cycle in addition to the outmost and its next cycles. And in the same cycle γ shows small difference. γ at $\theta = 0°$ is much smaller than that of $\theta = \theta_p$, and γ inclined to promote with size. The γ variations in Fig. 7–9 demonstrate that the magnitude of γ is strongly depend on the location of atom relative to the center and its stacking pattern with respect to six-membered ring in opposite layer. Atoms closer to the AA stacking tend to have smaller γ, while those closer to AB stacking and/or atoms in the outmost cycles tend to have larger γ.

4. Conclusion

In summary, we have carried out an in-depth theoretical investigation regarding the characteristic of interlayer polarizability and charge transfer in twisted bilayer graphene quantum dots driven by an external electric field. Our finding indicate that a relatively stable stacking pattern exists, which possesses the largest polarizability and its interlayer part, in contrast to the well-known Bernal stackings. The variation trends of band gap for the four studied sizes exhibit a six-fold rotating symmetry with a mirror symmetry of $\theta = 30°$. Furthermore, a quantity, α_{zz}^{Q}, is defined from electron density decomposition

and used to measure the interlayer polarizability effectively, dominating the variation of total polarizability with twisting angle. We have also verified the field-driven charge flow from one layer to another layer through the variations in α_{zz}^{Q}. α_{zz} and α_{zz}^{Q}, and charge transfer driven by an external field find their minimum at $\theta = 0°$ and largest values at size-dependent θ_p, which is corresponding to the AB stacking firstly appears at outmost cycle. By utilizing a derived equation with the relation between the GQD's diameter and twist angle, one can obtain the corresponding location for the appearance of largest α_{zz}, α_{zz}^{Q} and charge transfer. This allows one to predict the size of a TBG sample from the "magic angle" at which phenomena related to the largest polarizability appear. Moreover, our investigation also revealed that the largest atomic γ value is achieved at the outmost cycle for a specific angle and QD size. Our investigation on the size- and interlayer twist-mediated electric structure, polarizability and charge transfer characteristics in TBG QDs demonstrates that controlling the stacking pattern of layered-materials is a serviceable pathway to realize fascinating physicochemical and biological properties. Finally, similar twist-driven variations are noted for the coronene- and phenalenyl-based models. This study provides a deep theoretical insight on design and optimization of novel graphene-based devices to further extend their applications.

Author contributions

Xiangyue Liu: conceptualization, methodology, software, validation, writing – original draft, investigation, writing – review & editing, visualization. Xian Wang: investigation, writing – original draft. Shengping Yu: methodology, resources, project administration. Guangzhao Wang: investigation, methodology, supervision. Bing Li: resources, data curation, writing – review & editing, supervision. Tiantian Cui: investigation, methodology. Zhaoyang Lou: resources, data curation, writing – review & editing, supervision. Hong Ge: supervision, resources, project administration, funding acquisition, writing – review & editing.

Conflicts of interest

The authors declare no competing interests.

Acknowledgements

We acknowledge the support from the Scientific and Technological Project in Henan Province (grant no. 222102310015), and The Medical Science and Technology Project in Henan Province (grant no. SBGJ202102056).

References

1 H. Min and A. H. MacDonald, *Prog. Theor. Phys. Suppl.*, 2008, **176**, 227–252.
2 L. Banszerus, B. Frohn, A. Epping, D. Neumaier, K. Watanabe, T. Taniguchi and C. Stampfer, *Nano Lett.*, 2018, **18**, 4785–4790.
3 M. Eich, R. Pisoni, A. Pally, H. Overweg, A. Kurzmann, Y. Lee, P. Rickhaus, K. Watanabe, T. Taniguchi, K. Ensslin and T. Ihn, *Nano Lett.*, 2018, **18**, 5042–5048.
4 G. W. Burg, E. Khalaf, Y. Wang, K. Watanabe, T. Taniguchi and E. Tutuc, *Nat. Mater.*, 2022, **21**, 884–889.
5 J. M. Park, Y. Cao, L.-Q. Xia, S. Sun, K. Watanabe, T. Taniguchi and P. Jarillo-Herrero, *Nat. Mater.*, 2022, **21**, 877–883.
6 Y. Zhang, R. Polski, C. Lewandowski, A. Thomson, Y. Peng, Y. Choi, H. Kim, K. Watanabe, T. Taniguchi, J. Alicea, F. von Oppen, G. Refael and S. Nadj-Perge, *Science*, 2022, **377**, 1538–1543.
7 Y. Cao, D. Rodan-Legrain, O. Rubies-Bigorda, J. M. Park, K. Watanabe, T. Taniguchi and P. Jarillo-Herrero, *Nature*, 2020, **583**, 215–220.
8 Y. Cao, J. Luo, V. Fatemi, S. Fang, J. Sanchez-Yamagishi, K. Watanabe, T. Taniguchi, E. Kaxiras and P. Jarillo-Herrero, *Phys. Rev. Lett.*, 2016, **117**, 116804.
9 K. Kim, A. DaSilva, S. Huang, B. Fallahazad, S. Larentis, T. Taniguchi, K. Watanabe, B. J. LeRoy, A. H. MacDonald and E. Tutuc, *Proc. Natl. Acad. Sci. U. S. A.*, 2017, **114**, 3364–3369.
10 A. Kerelsky, L. McGilly, D. Kennes, L. Xian, M. Yankowitz, S. Chen, K. Watanabe, T. Taniguchi, J. Hone, C. Dean, A. Rubio and A. Pasupathy, *Nature*, 2019, **572**, 95.
11 M. V. Hosseini and M. Zareyan, *Phys. Rev. B: Condens. Matter Mater. Phys.*, 2012, **86**, 214503.
12 H. C. Po, L. Zou, A. Vishwanath and T. Senthil, *Phys. Rev. X*, 2018, **8**, 031089.
13 R. Bistritzer and A. H. MacDonald, *Proc. Natl. Acad. Sci. U. S. A.*, 2011, **108**, 12233–12237.
14 T. Ohta, A. Bostwick, T. Seyller, K. Horn and E. Rotenberg, *Science*, 2006, **313**, 951–954.
15 Y. Zhang, T.-T. Tang, C. Girit, Z. Hao, M. C. Martin, A. Zettl, M. F. Crommie, Y. R. Shen and F. Wang, *Nature*, 2009, **459**, 820–823.
16 S. Latil and L. Henrard, *Phys. Rev. Lett.*, 2006, **97**, 036803.
17 A. Gevaerd, C. E. Banks, M. F. Bergamini and L. H. Marcolino-Junior, *Electroanalysis*, 2019, **31**, 838–843.
18 D. Pan, J. Zhang, Z. Li and M. Wu, *Adv. Mater.*, 2010, **22**, 734–738.
19 K. A. Ritter and J. W. Lyding, *Nat. Mater.*, 2009, **8**, 235–242.
20 B. D. Mansuriya and Z. Altintas, *Sensors*, 2020, **20**, 1072.
21 P. Tian, L. Tang, K. S. Teng and S. P. Lau, *Mater. Today Chem.*, 2018, **10**, 221–258.
22 S. Chung, R. A. Revia and M. Zhang, *Adv. Mater.*, 2021, **33**, 1904362.
23 M. R. Younis, G. He, J. Lin and P. Huang, *Front. Chem.*, 2020, **8**, 424.
24 M. Nurunnabi, Z. Khatun, K. M. Huh, S. Y. Park, D. Y. Lee, K. J. Cho and Y.-K. Lee, *ACS Nano*, 2013, **7**, 6858–6867.
25 N. Abdullah Al, J. E. Lee, I. In, H. Lee, K. D. Lee, J. H. Jeong and S. Y. Park, *Mol. Pharmaceutics*, 2013, **10**, 3736–3744.
26 A. Xu, P. He, T. Huang, J. Li, X. Hu, P. Xiang, D. Chen, S. Yang, G. Wang and G. Ding, *Synth. Met.*, 2018, **244**, 106–112.

27 L. Lin, X. Song, Y. Chen, M. Rong, T. Zhao, Y. Wang, Y. Jiang and X. Chen, *Anal. Chim. Acta*, 2015, **869**, 89–95.
28 S. M. Ghafary, M. Nikkhah, S. Hatamie and S. Hosseinkhani, *Sci. Rep.*, 2017, **7**, 9552.
29 J. Ge, M. Lan, B. Zhou, W. Liu, L. Guo, H. Wang, Q. Jia, G. Niu, X. Huang, H. Zhou, X. Meng, P. Wang, C. S. Lee, W. Zhang and X. Han, *Nat. Commun.*, 2014, **5**, 4596.
30 F. Khodadadei, S. Safarian and N. Ghanbari, *Mater. Sci. Eng., C*, 2017, **79**, 280–285.
31 X. Wang, X. Sun, J. Lao, H. He, T. Cheng, M. Wang, S. Wang and F. Huang, *Colloids Surf., B*, 2014, **122**, 638–644.
32 Y. Yang, L. Zhang, J. Cai, X. Li, D. Cheng, H. Su, J. Zhang, S. Liu, H. Shi, Y. Zhang and C. Zhang, *ACS Appl. Mater. Interfaces*, 2016, **8**, 1718–1732.
33 J. Ruan, Y. Wang, F. Li, R. Jia, G. Zhou, C. Shao, L. Zhu, M. Cui, D.-P. Yang and S. Ge, *ACS Appl. Mater. Interfaces*, 2018, **10**, 14342–14355.
34 F.-I. Tung, L.-J. Zheng, K.-T. Hou, C.-S. Chiang, M.-H. Chen and T.-Y. Liu, *Nanoscale*, 2020, **12**, 8809–8818.
35 B. Trauzettel, D. V. Bulaev, D. Loss and G. Burkard, *Nat. Phys.*, 2007, **3**, 192–196.
36 S. Zhu, J. Zhang, C. Qiao, S. Tang, Y. Li, W. Yuan, B. Li, L. Tian, F. Liu, R. Hu, H. Gao, H. Wei, H. Zhang, H. Sun and B. Yang, *Chem. Commun.*, 2011, **47**, 6858–6860.
37 A. Kurzmann, M. Eich, H. Overweg, M. Mangold, F. Herman, P. Rickhaus, R. Pisoni, Y. Lee, R. Garreis, C. Tong, K. Watanabe, T. Taniguchi, K. Ensslin and T. Ihn, *Phys. Rev. Lett.*, 2019, **123**, 026803.
38 J. Berashevich and T. Chakraborty, *Phys. Rev. B: Condens. Matter Mater. Phys.*, 2011, **84**, 033403.
39 M. Mirzakhani, F. M. Peeters and M. Zarenia, *Phys. Rev. B*, 2020, **101**, 075413.
40 J. M. B. Lopes dos Santos, N. M. R. Peres and A. H. Castro Neto, *Phys. Rev. Lett.*, 2007, **99**, 256802.
41 J. B. Oostinga, H. B. Heersche, X. Liu, A. F. Morpurgo and L. M. K. Vandersypen, *Nat. Mater.*, 2008, **7**, 151–157.
42 E. V. Castro, K. S. Novoselov, S. V. Morozov, N. M. R. Peres, J. M. B. L. dos Santos, J. Nilsson, F. Guinea, A. K. Geim and A. H. C. Neto, *Phys. Rev. Lett.*, 2007, **99**, 216802.
43 M. Yankowitz, S. Chen, H. Polshyn, Y. Zhang, K. Watanabe, T. Taniguchi, D. Graf, A. F. Young and C. R. Dean, *Science*, 2019, **363**, 1059–1064.
44 B. Liu, Y. Sheng, S. Huang, Z. Guo, K. Ba, H. Yan, W. Bao and Z. Sun, *Chem. Mater.*, 2019, **31**, 6105–6109.
45 M. Huang and R. S. Ruoff, *Acc. Chem. Res.*, 2020, **53**, 800–811.
46 D. Pan, L. Guo, J. Zhang, C. Xi, Q. Xue, H. Huang, J. Li, Z. Zhang, W. Yu, Z. Chen, Z. Li and M. Wu, *J. Mater. Chem.*, 2012, **22**, 3314–3318.
47 S. Jindal and S. M. Giripunje, *Synth. Met.*, 2018, **239**, 36–42.
48 Y. Yang, J. Li, J. Yin, S. Xu, C. Mullan, T. Taniguchi, K. Watanabe, A. K. Geim, K. S. Novoselov and A. Mishchenko, *Sci. Adv.*, 2020, **6**, eabd3655.
49 X. Wang, L. Zhang, S. Yu, M. Yang and K. A. Jackson, *Phys. Rev. B*, 2021, **104**, 155411.
50 X. Wang and M. Yang, *Appl. Surf. Sci.*, 2022, **600**, 154148.
51 Y. Jiang, X. Lai, K. Watanabe, T. Taniguchi, K. Haule, J. Mao and E. Y. Andrei, *Nature*, 2019, **573**, 91–95.
52 B. Sahu, H. Min, A. H. MacDonald and S. K. Banerjee, *Phys. Rev. B: Condens. Matter Mater. Phys.*, 2008, **78**, 045404.
53 Q. Gao, Z. Zhang, X. Xu, J. Song, X. Li and Y. Wu, *Nat. Commun.*, 2018, **9**, 4778.
54 X. Wang, Y. Cui, L. Zhang and M. Yang, *Nano Res.*, 2021, **14**, 3935–3941.
55 T. Yanai, D. P. Tew and N. C. Handy, *Chem. Phys. Lett.*, 2004, **393**, 51–57.
56 S. Grimme, J. Antony, S. Ehrlich and H. Krieg, *J. Chem. Phys.*, 2010, **132**, 154104.
57 M. J. Frisch, J. A. Pople and J. S. Binkley, *J. Chem. Phys.*, 1984, **80**, 3265–3269.
58 F. L. Hirshfeld, *Theor. Chim. Acta*, 1977, **44**, 129–138.
59 A. Sagar, E. J. Lee, K. Balasubramanian, M. Burghard and K. Kern, *Nano Lett.*, 2009, **9**, 3124–3128.
60 V. Perebeinos, J. Tersoff and P. Avouris, *Phys. Rev. Lett.*, 2012, **109**, 236604.
61 Z.-H. Cui, H. Lischka, H. Z. Beneberu and M. Kertesz, *J. Am. Chem. Soc.*, 2014, **136**, 5539–5542.